

Random-Graph Models and Characterization of Granular Networks

Silvia Nauer,¹ Lucas Böttcher,^{1,2,*} and Mason A. Porter^{3,†}

¹*Institute for Theoretical Physics, ETH Zurich, 8093, Zurich, Switzerland*

²*Center of Economic Research, ETH Zurich, 8092, Zurich, Switzerland*

³*Department of Mathematics, University of California, Los Angeles, CA 90095, USA*

(Dated: February 15, 2022)

Various approaches and measures from network analysis have been applied to granular and particulate networks to gain insights into their structural, transport, failure-propagation, and other systems-level properties. In this paper, we examine a variety of common network measures and study their ability to characterize various two-dimensional and three-dimensional spatial random-graph models and empirical two-dimensional granular networks. We identify network measures that are able to distinguish between physically plausible and unphysical models that consist of randomly embedded and connected particles. Our results also suggest that there are significant differences in the distributions of certain network measures in two and three dimensions, hinting at important differences that we also expect to arise in experimental granular networks.

* lucasb@ethz.ch

† mason@math.ucla.edu

I. INTRODUCTION

Various tools from network analysis have been applied to gain further insights into transport, failure mechanisms, and other system-level properties of granular networks, which are typically constructed by interpreting the particles of the underlying packings as nodes and their contacts as edges [1–4]. Network analysis may help lead to better understanding and the ability to control fracture processes, design new materials, and assess structural degradation in various engineering applications [5–7]. Researchers have employed continuum [6] and particle-level [5, 8] descriptions to study granular materials [9, 10], but neither framework is designed to study intermediate-scale organization, which is important for understanding and characterizing granular packings [4, 11].

In the study of granular and particulate networks, it is not clear which network measures are most suitable for distinguishing between physical granular networks and randomly embedded and overlapping particle systems. To take advantage of methods of network analysis, it is necessary to identify appropriate network measures to best highlight the distinctions between different structures [12]. Building on ideas from Ref. [13], we compute a variety of common network diagnostics and apply them to several spatial network models and empirical granular networks in two and three dimensions. We identify measures that are able to distinguish between the network characteristics of physical and randomly embedded and overlapping particle systems. We test the convergence properties of our results by considering large ensembles of granular networks. Our results are relevant both for the study of granular networks and help provide a roadmap for useful ways to develop random-graph models for studying spatially-embedded networks (such as transportation, communication, and vascular systems). As has also been demonstrated in applications like sensor systems [14, 15], incorporating a small amount of physics into models such as random geometric graphs can provide important insights into the structure of such systems [12].

Our paper proceeds as follows. In Sec. II, we describe the network measures that we use in our investigation of spatial random graphs and granular networks. In Sec. III, we present several models of both unphysical and physical granular networks. The network structures range from random geometric graphs (RGGs) to physically plausible contact networks. To ensure comparability of our results with properties of real granular networks, we also apply our network measures to empirical granular network structures, and we generate our simulated networks according to empirically observed edge densities. We thereby examine if certain network measures are able to distinguish between clearly unphysical (i.e., overlapping) granular packings and ones that are potentially physically plausible. In Sec. IV, we compare the distributions of the network diagnostics on the various networks. We also examine the convergence properties of the considered network diagnostics by computing them for ensembles of large networks. In Sec. V, we conclude our study and discuss our results.

II. NETWORK DIAGNOSTICS

Networks have different characteristic features that depend on the processes and interactions that define them [16]. Many diagnostics have been developed to study and characterize networks, and we seek to use some of them to study granular networks and examine connections between network and particulate systems.

Consider a network $G(V, E)$, where V is a set of nodes and E is a set of edges. For each node $v \in V$, the degree $\deg(v)$ is the number of edges that are attached to v . For each node pair $\langle s, t \rangle \in V$, we denote a shortest path between s and t by $d_{\min}(s, t)$. We use σ_{st} to denote the number of shortest paths in the graph from s to t . The number of shortest paths from s to t that traverse $v \in V$ is $\sigma_{st}(v)$. Let $\sigma_{st}(e)$ denote the number of shortest paths from s to t that traverse an edge $e \in E$. We let $T(G)$ denote the number of triangles present in the graph. A triangle is a set of three nodes that are all pairwise connected by an edge. We denote the number of triangles that include a node $v \in V$ by $T(G; v)$. We count each triangle three times when computing the number of triangles in a graph G . All of the networks that we consider are unweighted and undirected, and we discuss several ways for characterizing them in the following paragraphs. To compute the values of these diagnostics, we use the Python library NETWORKX. See Ref. [17] for a detailed documentation.

a. Edge density. The edge density (or sometimes just “density”) of a network is

$$\rho = \frac{|E|}{|V|}, \quad (1)$$

where $|E|$ and $|V|$ are, respectively, the numbers of edges and nodes. We use edge density as reference measure for the construction of our networks. To compare the results of different network models, we first make sure that their edge densities are the same.

b. Geodesic node betweenness. The geodesic node betweenness centrality c_B for a node v is the sum (over all node pairs $\langle s, t \rangle$ in a network) of the number of shortest paths from s to t that traverse v divided by the total number

of shortest paths from s to t [16]. Including a normalization factor, we write geodesic node betweenness centrality as

$$c_B(v) = \sum_{\langle s,t \rangle \in V} \frac{\sigma_{st}(v)}{\sigma_{st}} \underbrace{\frac{2}{(|V|-1)(|V|-2)}}_{\text{normalization factor}}. \quad (2)$$

Note that $\sigma_{st} = 1$ if $s = t$ and that $\sigma_{st}(v) = 0$ if $v \in \{s, t\}$. We define a network's geodesic node betweenness

$$C_B(G) = \frac{1}{|V|} \sum_{v \in V} c_B(v) \quad (3)$$

as the mean of geodesic node betweenness centrality over all nodes in a network.

A large geodesic betweenness centrality $c_B(v)$ suggests that many shortest paths traverse a particular node. This may in turn suggest that such a node is relevant for transportation processes or failure-propagation mechanisms in granular networks [1–4].

c. Geodesic edge betweenness. We can also calculate a geodesic betweenness centrality for edges [18]:

$$c_B(e) = \sum_{\langle s,t \rangle \in V} \frac{\sigma_{st}(e)}{\sigma_{st}} \underbrace{\frac{2}{|V|(|V|-1)}}_{\text{normalization factor}}. \quad (4)$$

Based on Eq. (4), the geodesic edge betweenness of a network is

$$C_B(G) = \frac{1}{|E|} \sum_{e \in E} c_B(e). \quad (5)$$

d. Clustering coefficient. The local clustering coefficient $c(v)$ of a node v with degree $\deg(v) \geq 2$ is the number of triangles that include that node divided by all possible triangles that could include v (i.e., the connected triples) [16]. That is,

$$c(v) = \frac{2T(G; v)}{\deg(v)(\deg(v) - 1)}. \quad (6)$$

If the degree of a node is 0 or 1, the corresponding clustering coefficient of that node is 0. The mean local clustering coefficient of a network is

$$c(G) = \frac{1}{|V|} \sum_{v \in V} c(v). \quad (7)$$

e. Transitivity. Transitivity is the number of triangles in a network divided by the number of possible triangles [16]:

$$\text{Transitivity} = \frac{T(G)}{\text{Number of possible triangles in } G}. \quad (8)$$

Based on the definition of clustering coefficient and transitivity, we see that the two measures are closely related.

f. Degree assortativity. Degree assortativity is a measure to quantify the correlation between the degree of a certain node and the degrees of its neighbors [16]. Larger values of degree assortativity entail greater similarity in the degree of neighboring nodes. We compute degree assortativity by calculating a Pearson correlation coefficient, whose values lie in the interval $[-1, 1]$ [19]. A value of 1 indicates a network with perfect degree assortativity, a value of 0 corresponds to a nonassortative network, and a value of -1 indicates perfect degree disassortativity.

g. Global efficiency. The efficiency $E(u, v)$ of a node pair $\langle u, v \rangle$ is the inverse of the shortest-path length between these two nodes [20]. That is,

$$E(u, v) = \frac{1}{d_{\min}(u, v)}. \quad (9)$$

Global efficiency is the mean of the efficiencies over all pairs of nodes in a network:

$$E_{\text{glob}}(G) = \frac{1}{|\{\langle u, v \rangle \in V\}|} \sum_{\langle u, v \rangle \in V} E(u, v). \quad (10)$$

h. Local efficiency. The local efficiency [20] of a node v is

$$E_{\text{loc}}(v) = \frac{1}{|\langle u, w \rangle \in \Gamma(v)|} \sum_{\langle u, w \rangle \in \Gamma(v)} E(u, w), \quad (11)$$

where $\Gamma(v)$ denotes the neighborhood of v . The local efficiency of a network is

$$E_{\text{loc}}(G) = \frac{1}{|V|} \sum_{v \in V} E_{\text{loc}}(v), \quad (12)$$

the mean of the local efficiencies over all nodes of the network.

i. Mean shortest-path length in the largest connected component (LCC). The mean shortest-path length over all node pairs $\langle u, v \rangle$ of the largest connected component (LCC) C_{max} of a network is

$$\bar{d}_{\text{min}} = \frac{1}{|\{\langle u, v \rangle \in C_{\text{max}}\}|} \sum_{\langle u, v \rangle \in C_{\text{max}}} d_{\text{min}}(u, v). \quad (13)$$

j. Weighted mean shortest-path length. The weighted mean shortest-path length \bar{d}_{min}^w is the weighted arithmetic mean of the mean shortest-path lengths $\bar{d}_{\text{min}}(G_C)$ that we compute for connected components G_C of a graph. We use the number of nodes in each subgraph as a weight, so

$$\bar{d}_{\text{min}}^w = \frac{1}{|V|} \sum_{G_C \in G} \bar{d}_{\text{min}}(G_C) |G_C|, \quad (14)$$

where $|G_C|$ denotes the number of nodes in the considered connected component.

k. Maximized modularity. Subgraphs of a network G are often called “communities” in the context of dense sets of nodes that are connected sparsely to other dense sets of nodes [21, 22]. Given a set of communities of a network G , the modularity $Q \in [-1, 1]$ measures the density of edges (adjusted for edge weights) inside communities compared to edges between communities [23]. For an unweighted graph, the modularity Q of a partition of a graph G is

$$Q = \frac{1}{2|E|} \sum_{\langle u, v \rangle \in G} \left[A_{uv} - \frac{\deg(u)\deg(v)}{2|E|} \right] \delta(G_{C_u}, G_{C_v}), \quad (15)$$

where A is the adjacency matrix of the network, δ is the Kronecker delta, and G_{C_u} denotes the community that includes node u .

We maximize modularity by applying the locally greedy Louvain method for community detection [23]. Maximized modularity measures how well one can partition a network into non overlapping communities [21].

l. Subgraph centrality. For a node v and an adjacency matrix A associated with the graph G , the subgraph centrality [24]

$$S(v) = \sum_{k=0}^{\infty} \frac{(A^k)_{vv}}{k!} \quad (16)$$

is the sum of weighted closed walks (of all lengths) that start and end at node v . Instead of weighting each term with $1/k!$, other choices of the weights are also possible. The elements (u, v) of the matrix powers A^k have the following interpretation: each element (u, v) represents the number of paths of length k from node u to node v . The mean subgraph centrality in a network G is

$$S(G) = \frac{1}{|V|} \sum_{v \in V} S(v). \quad (17)$$

m. Communicability. The communicability between nodes u and v is [25]

$$C_{\text{com}}(u, v) = \sum_{k=1}^{\infty} \frac{(A^k)_{uv}}{k!}, \quad (18)$$

so it measures the number of closed walks between nodes u and v .

The communicability of a network G is the mean of the communicabilities between all pairs of nodes in the network:

$$C_{\text{com}}(G) = \frac{1}{|\{\langle u, v \rangle \in V\}|} \sum_{\langle u, v \rangle \in V} C_{\text{com}}(u, v). \quad (19)$$

From the definitions above, we see that many of the diagnostic values depend on the number of nodes in a network. Therefore, we set the number of nodes in each the models that we study to be equal to the one of the experimental data. This allows us to compare the resulting diagnostics for our models and the empirical granular networks.

III. RANDOM-GRAPH MODELS OF GRANULAR NETWORKS

As baselines to compare to empirical granular networks, we consider various models of spatial networks in two and three dimensions. We start with random geometric graphs (RGGs), which is an unphysical model, and then we examine some more realistic models (such as force-modified RGGs). After discussing these models in two dimensions, we also examine some models in three dimensions. The reason for studying different models, ranging from unphysical ones to more physical ones, is that we aim at identifying diagnostics that are able to capture properties of realistic granular networks, which consist of non-overlapping particles [13]. The model networks also allow us to analyze the convergence properties of different network measures, because we can generate large numbers of different network configurations and examine how they behave when they consist of progressively more nodes. We also apply our network measures to two-dimensional empirical granular networks and use the empirically determined edge densities as input for our granular network models in two dimensions. Given a specific edge density, we perform all of the computations for the same configuration as in the experimental case (see Sec. III E). Specifically, the empirical granular systems are confined by a two-dimensional box with dimensions 290 mm \times 380 mm and have a mean of 1122 particles. For the three-dimensional materials, we examine model networks with 1122 particles in a box of dimensions 102 mm \times 102 mm \times 102 mm.

A. Random geometric graphs (RGGs)

As a first, overly simplistic model of a granular system, we consider a monodisperse RGG. In this model, we place n particles (represented by nodes) uniformly at random with the same radius r in the box. The nodes are adjacent if the distance between them is smaller than $2R$, where we choose the parameter R based on the edge density that matches an empirical granular network that we will study later (see Sec. III E). Because of the possibility of multiple overlapping particles, this monodisperse RGG is not a good model of a physical granular system. We also consider a bidisperse RGG. In this model, the particles can have two different radii, r_1 and r_2 ; and nodes i and j are adjacent to each other if their distance is smaller than $R(r_i + r_j)$. For each particle, we generate a uniformly distributed random number $\epsilon \sim \mathcal{U}(0, 1)$. If $\epsilon < 0.5$, we set the particle radius to r_1 ; otherwise, we set it to r_2 . We use the same procedure for all bidisperse models in this paper. We want 50%, on average, of particles to have radius r_1 to facilitate our comparison with the employed experimental granular network data (see Sec. III E). As in the monodisperse case, we place particles uniformly at random. In this case as well, we need to choose R to match a desired edge density. We show examples of both a monodisperse and a bidisperse RGG in Fig. 1.

The parameters in our computations are $n = 1122$ nodes, a radius of $r = 4.5$, and a distance parameter of $R \approx 5.69$ for the monodisperse RGG and $n = 1122$, $r_1 = 4.5$, $r_2 = 5.5$, and $R = 1.13$ for the bidisperse RGG.

B. Proximity-modified random geometric graphs

To compensate for some of the overlaps between particles in an RGG, we now define a proximity measure p that describes the distance between each point (x, y) and its nearest particle(s). Initially, the system is empty. We then place each particle as follows. For each integer $k \in \{1, \dots, n\}$, we place particle k with radius r_k in the box. To do this, we choose a position (x_k, y_k) in the box uniformly at random, and we place the particle with probability

$$P(p_k) = \begin{cases} 0, & \text{for } p_k < 2\alpha r_k, \\ 1, & \text{for } p_k \geq 2\alpha r_k, \end{cases} \quad (20)$$

where p_k is the proximity for the position (x_k, y_k) and $\alpha \in [0, 1]$ is a parameter that enforces a maximum particle density in a given area. We use this procedure for both monodisperse ($r_k = r$) and bidisperse ($r_k \in \{r_1, r_2\}$) particle configurations. We generate the edges in the same way as in the bidisperse RGG model.

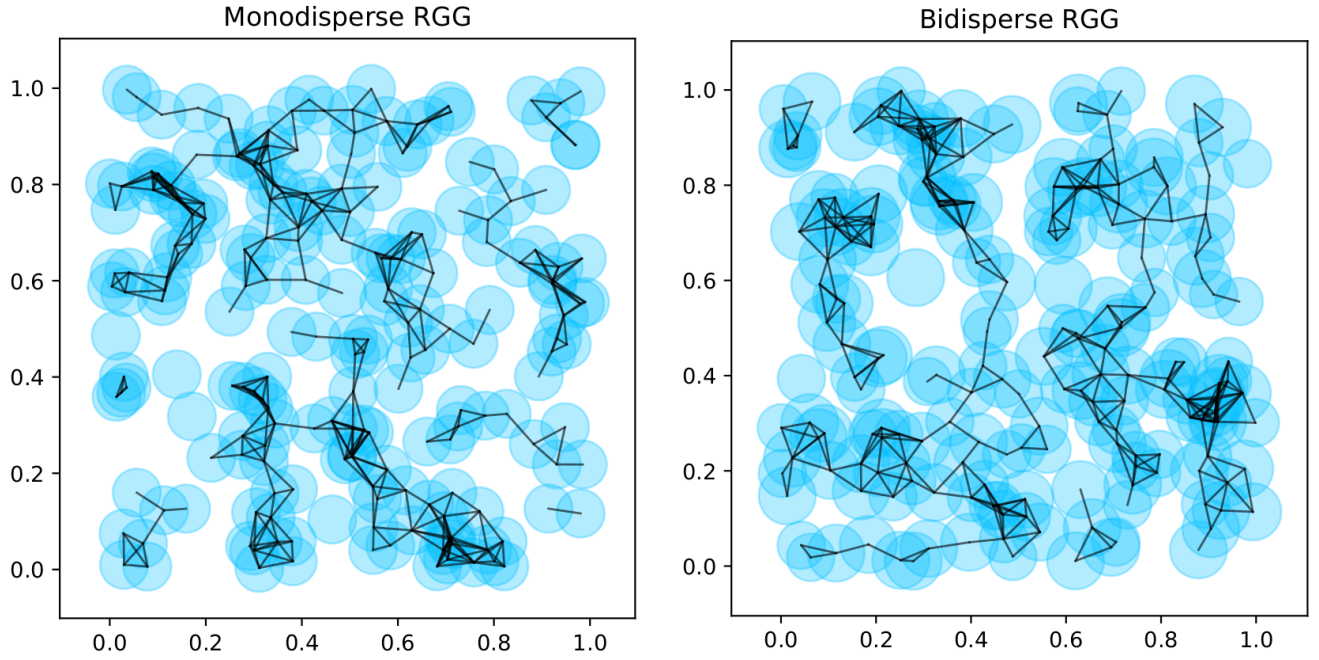


Figure 1. **(Left) Monodisperse and (right) bidisperse random geometric graph in the unit square.** The monodisperse RGG has $n = 200$ nodes, particles of radius $r = 0.05$, and a distance parameter of $R \approx 0.0428$; and the bidisperse RGG has $n = 200$ nodes, particles of radius $r_1 = 0.05$ and $r_2 = 0.06$ (there are 92 of radius r_1 and 108 particles of radius r_2), and a distance parameter of $R \approx 0.7770$. In the bidisperse case, we generate a uniformly distributed random number $\epsilon \sim \mathcal{U}(0, 1)$ for each particle. If $\epsilon < 0.5$, we set the particle radius to r_1 ; otherwise, we set it to r_2 .

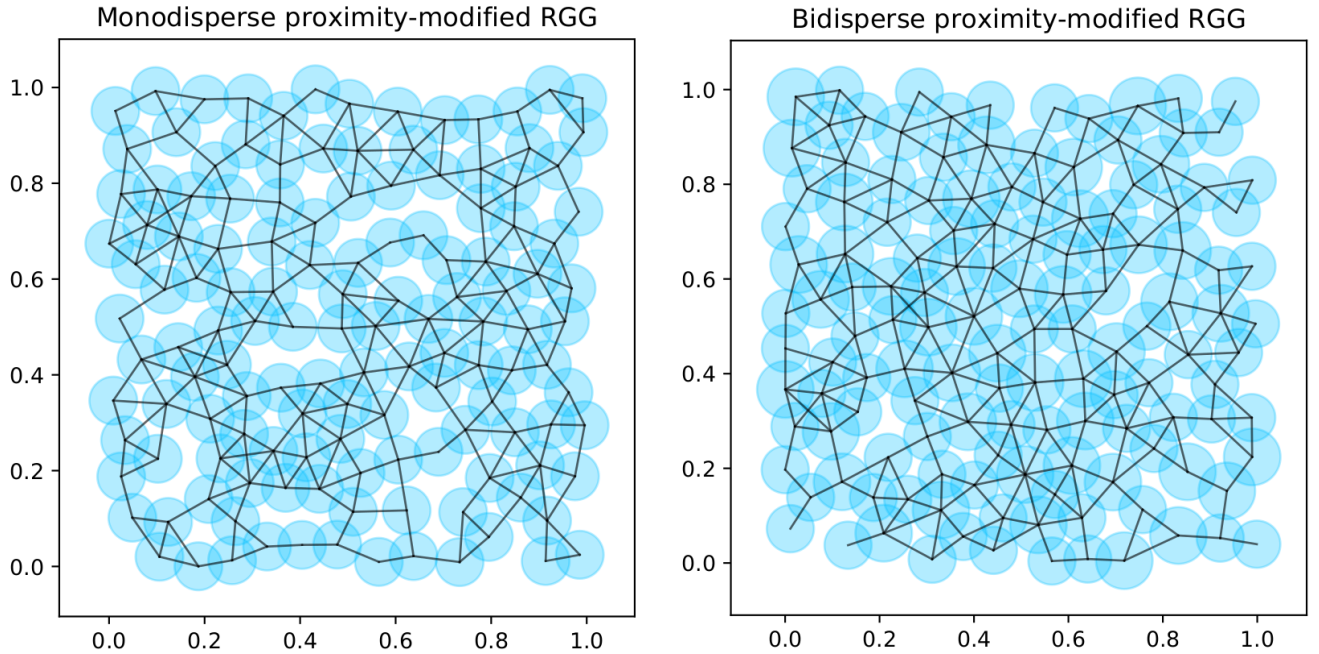


Figure 2. **Monodisperse and bidisperse proximity-modified RGGs in the unit square.** The parameters are $n = 135$, $r = 0.05$, $\alpha = 0.7$, and $R \approx 0.0588$ for the monodisperse example and $n = 135$, $r_1 = 0.05$, $r_2 = 0.06$ (there are 90 of radius r_1 and 45 particles of radius r_2), $\alpha = 0.7$, and $R \approx 1.1020$ for the bidisperse example. The parameter α enforces a maximum particle density in a given area. In the bidisperse case, we generate a uniformly distributed random number $\epsilon \sim \mathcal{U}(0, 1)$ for each particle. If $\epsilon < 0.5$, we set the particle radius to r_1 ; otherwise, we set it to r_2 .

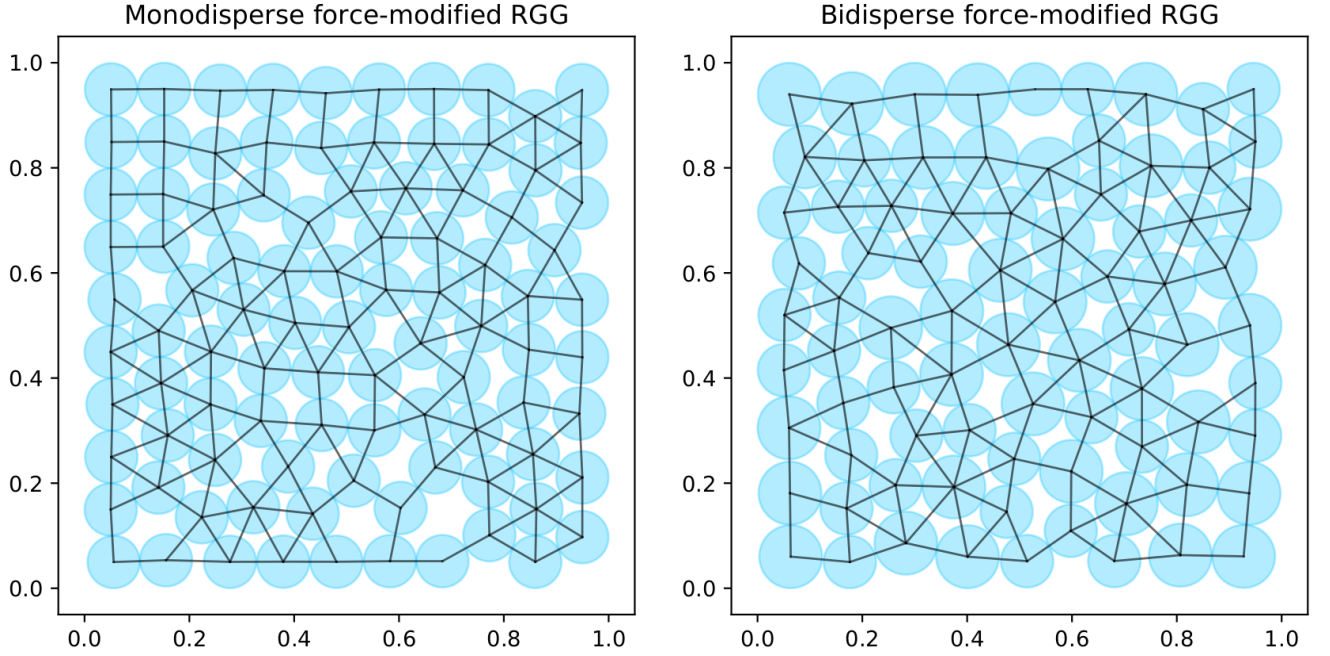


Figure 3. **Monodisperse and bidisperse force-modified RGGs in the unit square.** The parameters are $n = 95$, $r = 0.05$, $\beta = 0.5$, and $R = 0.0615$ (monodisperse) and $n = 80$, $r_1 = 0.05$, $r_2 = 0.06$ (there are 41 of radius r_1 and 39 particles of radius r_2), $\beta = 0.5$, and $R \approx 1.2280$ (bidisperse). To generate these configurations, we update the positions \mathbf{x}_k of all particles 700 times using $\mathbf{x}_k \rightarrow \mathbf{x}_k + \mathbf{d}_k$. The displacement \mathbf{d}_k is proportional to the force \mathbf{f}_k defined by Eq. (21), and the parameter β gives the exponent in the force law. In the bidisperse case, we generate a uniformly distributed random number $\epsilon \sim \mathcal{U}(0, 1)$ for each particle. If $\epsilon < 0.5$, we set the particle radius to r_1 ; otherwise, we set it to r_2 .

In Fig. 2, we show a monodisperse and a bidisperse proximity-modified RGG. Based on the depicted configurations, we see that the proximity-modified RGG exhibits fewer overlaps than a standard RGG. However, overlaps are still present, so the model does not describe a physical granular network.

For our computations, we use the parameters $n = 1122$, $r = 4.5$, $\alpha = 0.75$, and $R \approx 1.39$ for the monodisperse case and $n = 1122$, $r_1 = 4.5$, $r_2 = 5.5$, $\alpha = 0.75$, and $R \approx 1.24$ for the bidisperse case. In the bidisperse case, we generate a uniformly distributed random number $\epsilon \sim \mathcal{U}(0, 1)$ for each particle. If $\epsilon < 0.5$, we set the particle radius to r_1 ; otherwise, we set it to r_2 .

C. Force-modified random geometric graphs

To obtain a network whose characteristics better resemble those of a physical granular packing, we now apply a different modification to the RGG. Initially, we start from an RGG configuration. For each particle k , we use a Hertzian-like contact theory [26] to compute the force \mathbf{f}_k that acts on it from overlaps with other particles. After computing the forces \mathbf{f}_k , we update the corresponding locations \mathbf{x}_k according to $\mathbf{x}_k \rightarrow \mathbf{x}_k + \mathbf{d}_k$, with $\mathbf{d}_k = \epsilon \mathbf{f}_k$. We repeat this process until the particles no longer overlap (see Appendix A). One can use the parameter ϵ to rescale the displacements \mathbf{d}_k that may be too large and potentially lead to new overlaps if they are not reduced. For a box of dimensions $L_x \times L_y$ and according to Hertzian contact theory, the force on particle k is [26, 27]

$$\mathbf{f}_k = \sum_{l \neq k} \left\{ \left[\frac{1}{2}(r_k + r_l) - \frac{1}{2}|\mathbf{x}_k - \mathbf{x}_l| \right]_+^\beta \frac{\mathbf{x}_k - \mathbf{x}_l}{|\mathbf{x}_k - \mathbf{x}_l|} \right\} + [r_k - x_k]_+^\beta \hat{\mathbf{x}} - [r_k + x_k - L_x]_+^\beta \hat{\mathbf{x}} + [r_k - y_k]_+^\beta \hat{\mathbf{y}} - [r_k + y_k - L_y]_+^\beta \hat{\mathbf{y}}, \quad (21)$$

where the exponent β (which is $\beta = 3/2$ in classical Hertzian theory, but was estimated to be $\beta = 5/4$ for the 2D granular material in [26]) describes the interaction strength between particles. The vectors $\hat{\mathbf{x}}$ and $\hat{\mathbf{y}}$ are the unit vectors in the x and y directions, respectively. Forces occur only between overlapping particles or between a particle

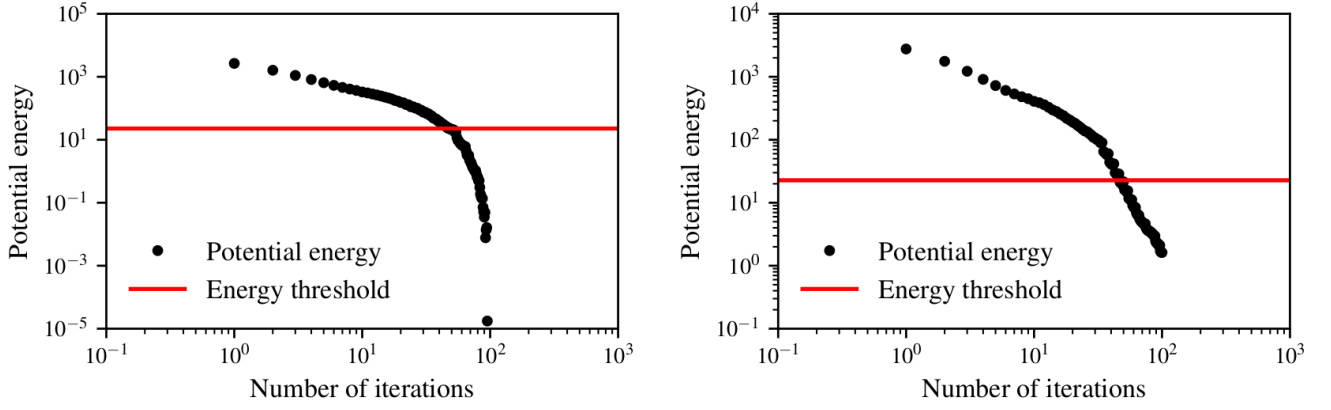


Figure 4. **Energy convergence for the monodisperse force-modified RGG model.** We generate RGGs using the parameter values $n = 1122$, $r = 4.5$, $\beta = 0.5$, and $R \approx 1.29$ for a box with dimensions $L_x = 290$ and $L_y = 380$. For both of our examples, we update the positions \mathbf{x}_k of all particles 100 times using $\mathbf{x}_k \rightarrow \mathbf{x}_k + \mathbf{d}_k$. The displacement \mathbf{d}_k is proportional to the force \mathbf{f}_k defined by Eq. (21). The left panel shows an example in which the energy approaches 0, and the right panel shows an example in which the energy does not approach 0 but is smaller than some threshold (given by the red solid line) that we choose such that there are no visible overlaps between particles (see Appendix A).

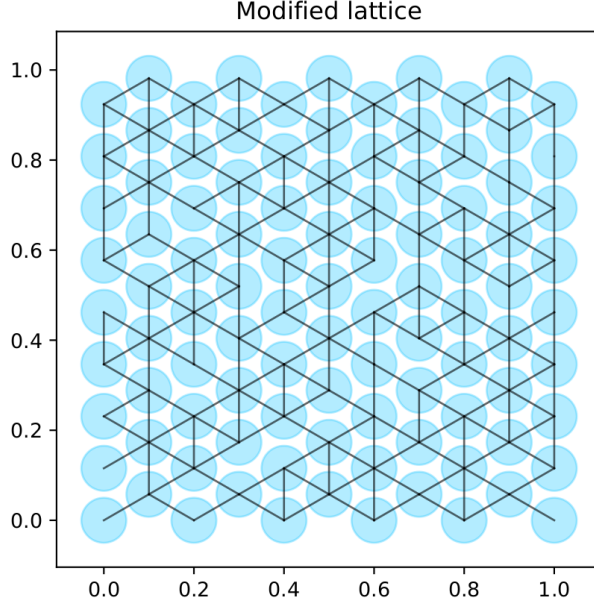


Figure 5. **Modified lattice in the unit square.** We consider 5×4 centers of hexagons, particles of radius, $r = 0.05$, and a removal fraction of $\mu \approx 0.1870$.

and the box boundary if both are in contact. Therefore, the bracket $[x]_+$ in Eq. (21) is

$$[x]_+ = \begin{cases} x, & \text{for } x > 0, \\ 0, & \text{for } x \leq 0. \end{cases} \quad (22)$$

The potential energy that corresponds to (21) is

$$V = \sum_k \sum_{l \neq k} \left\{ \left[\frac{1}{2}(r_k + r_l) - \frac{1}{2}|\mathbf{x}_k - \mathbf{x}_l| \right]_+^{\beta+1} \right\} + [r_k - x_k]_+^{\beta+1} - [r_k + x_k - L_x]_+^{\beta+1} + [r_k - y_k]_+^{\beta+1} - [r_k + y_k - L_y]_+^{\beta+1}. \quad (23)$$

The first term of Eqs. (21) and (23) accounts for overlaps between particles, and the other terms take into account the left, right, lower, and upper boundaries of the box. We generate the edges in this model as we did for bidisperse RGGs. We show examples of monodisperse and bidisperse force-modified RGGs in Fig. 3. In this figure, it appears (based on visual inspection) that particles do not overlap anymore. At least visually, they more closely resemble real granular networks.

To ensure that our final configurations are free of overlaps, we monitor their energy. If the energy approaches 0, there are no overlaps, and we stop updating locations. However, in some cases, the energy does not approach 0, because some particles are locally jammed [28]. In such cases, we accept a configuration if its energy is smaller than the energy of a system in which every particle k has an overlap distance of no more than $r_k/200$ with all of its neighbors. In Fig. 4, we show the monitored energy for two cases of the monodisperse force-modified RGG. A situation in which every particle overlaps with all of its neighbors is unlikely to occur. Instead, there are often some particles that overlap with one or two neighbors with a large fraction of their areas. To avoid large overlaps, we also check for every configuration that each of its particles k do not have an overlap distance with one of the neighbors that is larger than $r_k/15$. See Appendix A for details.

The parameters in our computations are $n = 1122$, $r = 4.5$, $\beta = 0.5$, $L_x = 290$, $L_y = 380$, and $R \approx 1.2900$ for the monodisperse case. For the bidisperse case, they are $n = 1122$, $r_1 = 4.5$, $r_2 = 5.5$, $\beta = 0.5$, $L_x = 290$, $L_y = 380$, and $R \approx 1.0850$. To generate these configurations, we perform 100 iterations for the monodisperse case and 400 iterations for the bidisperse one. As in the RGG model, 50% of the particles, on average, in the bidisperse case have a radius of r_1 ; and the others have a radius of r_2 .

D. Modified lattice

We also consider a modified lattice. In this model, we modify a hexagonal lattice of particles of the same radii by removing a fraction μ of edges uniformly at random to match a certain edge density. We show an example of a modified lattice in Fig. 5. In our computations, we use a total of 15×17 central hexagon particles, and we set $r = 4.5$ and $\mu \approx 0.26$.

E. Experimental data

To compare our model networks with real granular networks, we extract granular networks from experimental data [29]. Henceforth, when we write “experimental data”, we mean data from a bidisperse granular system with radii $r_1 = 4.5$ mm and $r_2 = 5.5$ mm in a two-dimensional box with side lengths $l_1 = 290$ mm and $l_2 = 380$ mm. The employed experimental data set consists of 17 different configurations of granular networks. We compute the diagnostics of Sec. II for these 17 cases, and we present the corresponding diagnostic values in Appendix B. On average, the number of particles in the experimental configurations is 1122, and 49.2% of the particles have a radius of r_1 . Therefore, we use 1122 particles in our model networks to facilitate comparisons between our models and the experimental data. For the bidisperse network models, we generate a uniformly distributed random number $\epsilon \sim \mathcal{U}(0, 1)$. If $\epsilon < 0.5$, we set the particle radius to r_1 ; otherwise, we set it to r_2 . We consider bidisperse packings, as we wish to avoid the crystallization of monodisperse packings. We show an example of the experimental setup in Fig. 6. To get this kind of configuration, about 1000 particles (which were cut from Vishay PSM-4 photoelastic material) were placed into a container with an open top, such that the particles were confined only by gravity [29].

F. Models in 3D

As with the 2D examples, we calculate the network diagnostics of Sec. II for 3D granular networks. In this section, we briefly discuss the extension of the previously-discussed models to 3D. The RGG model requires no special modification for the generation of the configurations, although the underlying box is now in 3D. We show examples of 3D monodisperse and bidisperse RGGs in the top panels of Fig. 7. As in the 2D RGGs, we observe that the particles overlap, so the model is not physical. Our parameters for these models are $n = 1122$, $r = 4.5$, and $R \approx 6.0750$ for the monodisperse case and $n = 1122$, $r_1 = 4.5$, $r_2 = 5.5$, and $R \approx 1.1950$ for the bidisperse case. As in the 2D models, 50% of the particles in our 3D models have radius r_1 on average and the others have radius r_2 .

The extension of the proximity-modified RGG to 3D is also straightforward. We show examples of 3D monodisperse and bidisperse proximity-modified RGGs in the bottom panels of Fig. 7. We see that the particles overlap less than for the unmodified 3D RGGs, but they still overlap. To obtain these configurations, we use the parameters $n = 1122$,

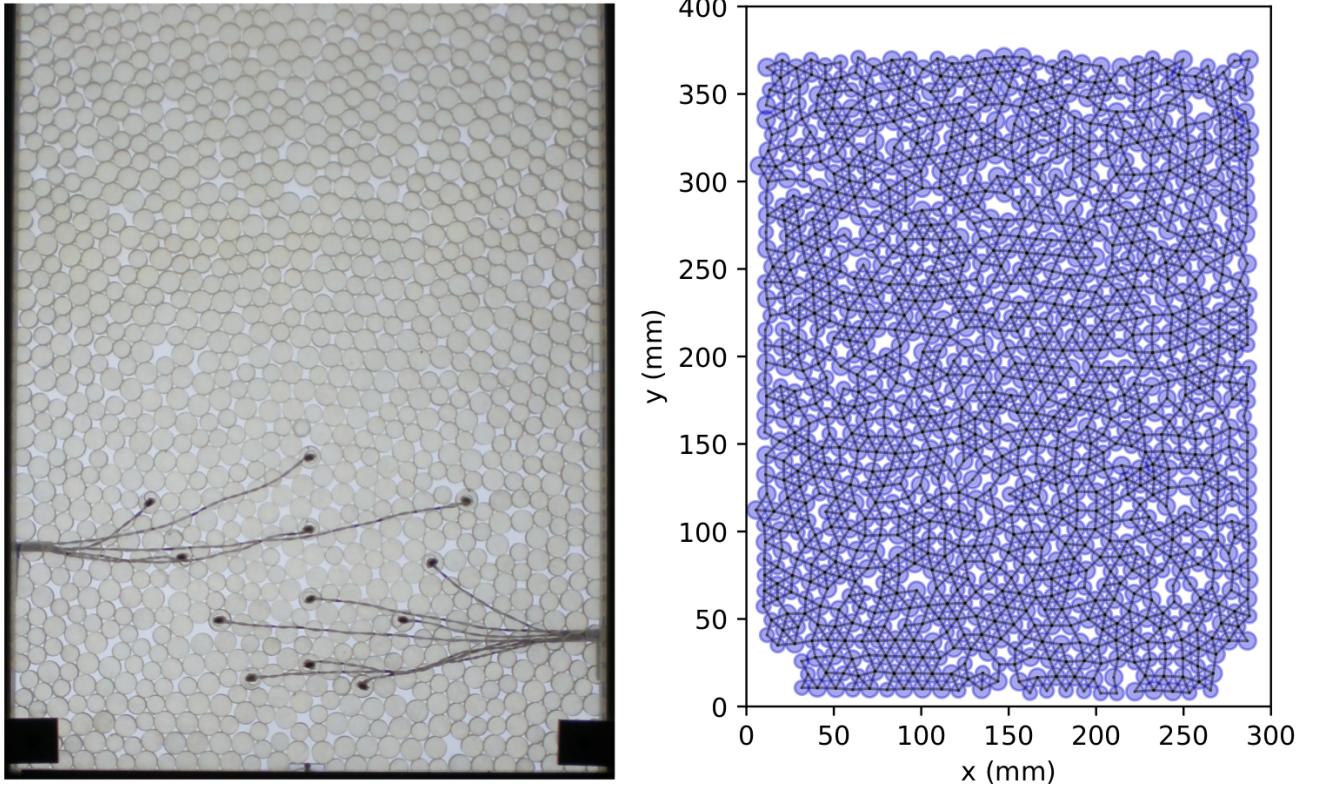


Figure 6. **Experimental granular network.** The particles have radii $r_1 = 4.5$ mm and $r_2 = 5.5$ mm, and the box has sides of lengths $l_1 = 290$ mm and $l_2 = 380$ mm. In the left panel, we show the experimental setup; in the right panel, we show the corresponding extracted granular network. The data is taken from Ref. [29].

$r = 4.5$, $\alpha = 0.75$, and $R \approx 1.4200$ for the monodisperse case and $n = 1122$, $r_1 = 4.5$, $r_2 = 5.5$, $\alpha = 0.75$, and $R \approx 1.4385$ for the bidisperse case.

For the force-modified RGG, we have to adapt Eqs. (21) and (23) to 3D. Equation (21) becomes

$$\begin{aligned} \mathbf{f}_k = \sum_{l \neq k} \left\{ \left[\frac{1}{2}(r_k + r_l) - \frac{1}{2}|\mathbf{x}_k - \mathbf{x}_l| \right]_+^\beta \frac{\mathbf{x}_k - \mathbf{x}_l}{|\mathbf{x}_k - \mathbf{x}_l|} \right\} \\ + [r_k - x_k]_+^\beta \hat{\mathbf{x}} - [r_k + x_k - L_x]_+^\beta \hat{\mathbf{x}} + [r_k - y_k]_+^\beta \hat{\mathbf{y}} - [r_k + y_k - L_y]_+^\beta \hat{\mathbf{y}} \\ + [r_k - z_k]_+^\beta \hat{\mathbf{z}} - [r_k + z_k - L_z]_+^\beta \hat{\mathbf{z}}, \end{aligned} \quad (24)$$

where $\hat{\mathbf{z}}$ denotes the unit vector in the z direction. Equation (23) becomes

$$\begin{aligned} V = \sum_k \sum_{l \neq k} \left\{ \left[\frac{1}{2}(r_k + r_l) - \frac{1}{2}|\mathbf{x}_k - \mathbf{x}_l| \right]_+^{\beta+1} \right\} \\ + [r_k - x_k]_+^{\beta+1} - [r_k + x_k - L_x]_+^{\beta+1} + [r_k - y_k]_+^{\beta+1} - [r_k + y_k - L_y]_+^{\beta+1} \\ + [r_k - z_k]_+^{\beta+1} - [r_k + z_k - L_z]_+^{\beta+1}. \end{aligned} \quad (25)$$

We show examples of 3D force-modified RGGs in the top panels of Fig. 8. As in the 2D case, based on visual inspection, we conclude that they resemble real granular networks more closely than the other models. The parameters in our computations are $n = 1122$, $r = 4.5$, $\beta = 0.5$, and $R \approx 1.4080$ for the monodisperse case and $n = 1122$, $r_1 = 4.5$, $r_2 = 5.5$, $\beta = 0.5$, and $R \approx 1.2600$ for the bidisperse case. In both examples, we set $L_x = L_y = L_z = 102$. To generate these configurations, we perform 100 iterations for the monodisperse case and 400 iterations for the bidisperse one. We describe the energy thresholds for the 3D force-modified RGGs in Appendix A.

We extend the modified lattice to 3D by considering a hexagonal packing of spherical particles. We create the edges in the same way as in the 2D modified lattice. In the bottom panel of Fig. 8, we show an example of a 3D modified

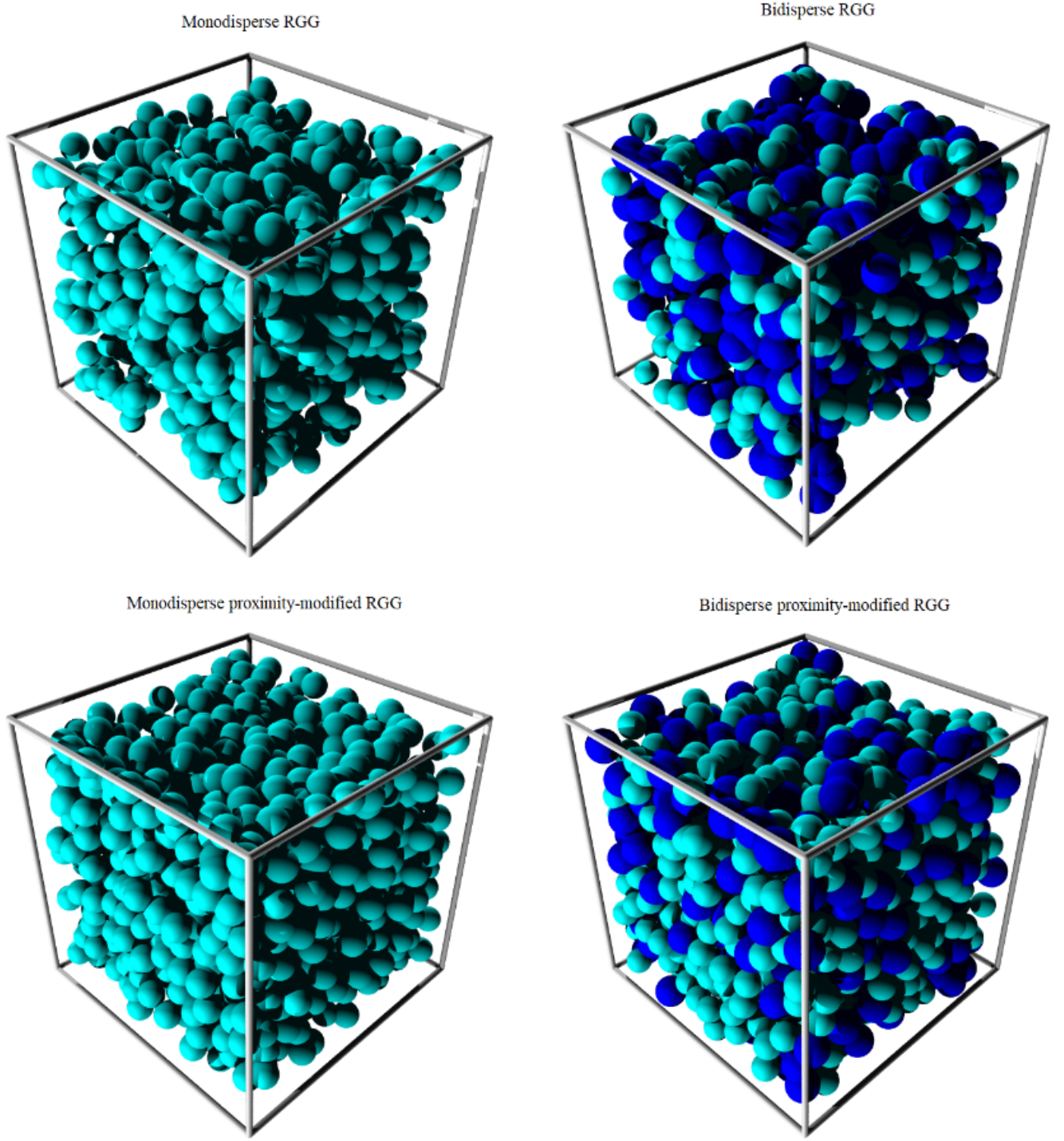


Figure 7. **Three-dimensional RGG and proximity-modified RGG models.** The parameters for the ordinary RGGs are $n = 1122$, $r = 4.5$, and $R \approx 6.0750$ for the monodisperse case and $n = 1122$, $r_1 = 4.5$, $r_2 = 5.5$, and $R \approx 1.1950$ for the bidisperse case. For the proximity-modified RGG models, the parameters are $n = 1122$, $r = 4.5$, $\alpha = 0.75$, and $R \approx 1.4200$ for the monodisperse case and $n = 1122$, $r_1 = 4.5$, $r_2 = 5.5$, $\alpha = 0.75$, and $R \approx 1.4385$ for the bidisperse cases. In the bidisperse case, we generate a uniformly distributed random number $\epsilon \sim \mathcal{U}(0, 1)$ for each particle. If $\epsilon < 0.5$, we set the particle radius to r_1 ; otherwise, we set it to r_2 . In all four examples, we consider a box of dimensions $L_x \times L_y \times L_z = 102 \times 102 \times 102$.

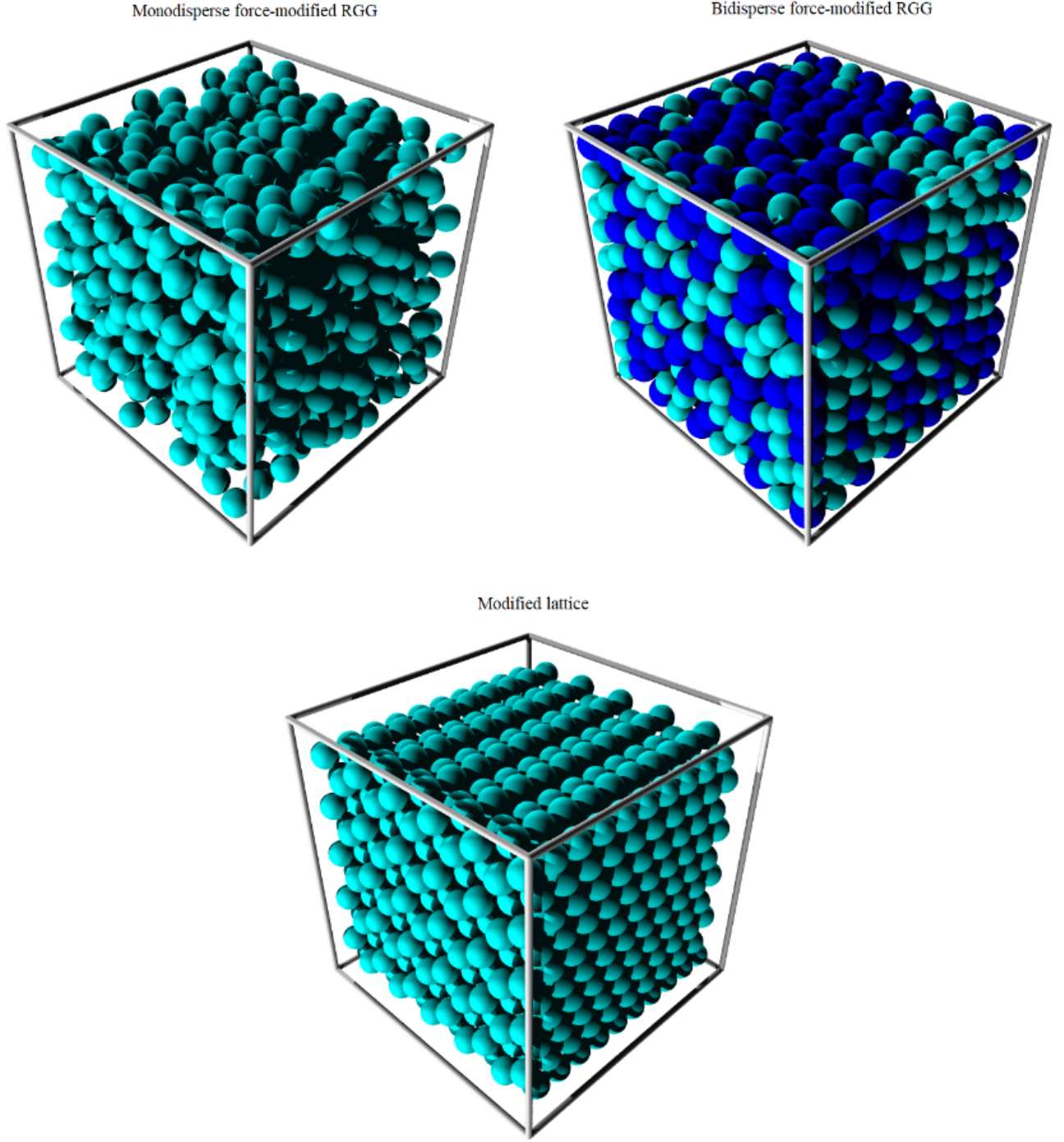


Figure 8. **Three-dimensional force-modified RGG and modified lattice models.** The parameters for the force-modified RGG models are $n = 1122$, $r = 4.5$, $\beta = 0.5$, and $R \approx 1.4080$ for the monodisperse case and $n = 1122$, $r_1 = 4.5$, $r_2 = 5.5$, $\beta = 0.5$, and $R \approx 1.2600$ for the bidisperse case. To generate these configurations, we update the positions \mathbf{x}_k of all particles 100 times for the monodisperse case and 400 times for the bidisperse case according to $\mathbf{x}_k \rightarrow \mathbf{x}_k + \mathbf{d}_k$. The displacement \mathbf{d}_k is proportional to the force \mathbf{f}_k defined by Eq. (24). For the modified lattice, we arrange 1100 particles of radius $r = 4.5$ in a hexagonal packing and we set $\mu \approx 0.4950$. In the bidisperse case, we generate a uniformly distributed random number $\epsilon \sim \mathcal{U}(0, 1)$ for each particle. If $\epsilon < 0.5$, we set the particle radius to r_1 ; otherwise, we set it to r_2 . In all cases, we consider a box of dimensions $L_x \times L_y \times L_z = 102 \times 102 \times 102$.

lattice that consists of 1100 particles. The particles have a radius of $r = 4.5$, and we remove a fraction $\mu \approx 0.4950$ of the edges uniformly at random from the network.

IV. RESULTS

A. Diagnostics for 2D granular networks

We first focus on the results of calculating the network diagnostics for the 2D models from Sec. III. We describe the convergence characteristics of all diagnostics and then discuss the distributions of several of them.

1. Convergence characteristics

To monitor the convergence of the diagnostics, we generate 10 ensembles with different numbers of granular-network configurations. Specifically, ensemble m has 2^m networks (where $m \in \{0, \dots, 9\}$), so there are 1023 networks in total. For each m , we compute the mean of the diagnostic values and normalize each value by the mean that we calculate for $m = 9$. Therefore, each of the mean diagnostic values approaches 1 for $m = 9$ (see Fig. 9). This procedure allows us to identify a reasonable number of networks such that the deviations of the mean diagnostic values are sufficiently small in comparison to the values in the largest ensemble. We thereby study the convergence properties of the mean diagnostic values with respect to the values in the largest ensemble. Based on the data in Fig. 9, we see that the diagnostics behave differently in the different network models.

In the unmodified RGG models, some of the normalized mean diagnostics deviate more from 1 than in the other models. We observe this behavior for geodesic node betweenness, geodesic edge betweenness, subgraph centrality, and communicability. Because we place the particles in the RGGs uniformly at random, different configurations can differ substantially from each other. For example, in our computations, we observe that some particle configurations have local accumulations of particles, and such outliers strongly influence the mean over ensembles with a small number of networks. Such outliers exert less influence for ensembles with many networks, so they have a smaller effect on those ensembles. For the aforementioned diagnostics, such particle accumulations in some samples lead to the clearly visible zigzag behavior in Fig. 9. In the other network models, this issue is less prominent, because local particle accumulations are suppressed by the proximity and force modifications. The larger deviations of the mean diagnostics in the unmodified RGG models is also reflected by their distributions (see Sec. IV A 3). For the proximity-modified RGG and the force-modified RGG, the mean diagnostic values approach the value that we observe in the largest ensemble faster than in the unmodified RGG models. For the modified-lattice model, we observe that almost all mean diagnostic curves are constant; the only exception is degree assortativity. In this model, the only process that has any randomness is deleting edges from the initially-complete hexagonal packing.

2. Numerical values

We summarize the diagnostic values for the models and experimental granular networks in Appendix B. For each model, our results are means over all 1023 configurations that we generated to study the convergence characteristics of the diagnostics in Sec. IV A 1. For the experimental data, we take means over the 17 network realizations.

Based on the numbers in Tables I and II in Appendix B, we note several differences between our models. From the results, it is clear that the RGG is the most unphysical of these models; we already made this point when visualizing an associated particle system. The proximity-modified RGG has diagnostic values that resemble the experimental values more closely, and the force-modified RGG generates the most realistic configurations. The results of the modified-lattice model agree partly with the experimental data, but they are not better than the force-modified RGG values and values of degree assortativity in the modified lattice differ significantly from those in the experimental configurations. The modified lattices are also visually rather different from the experimental packings, as noted in [13]. A closer look at the diagnostics of the bidisperse force-modified RGG reveals that it is the model that best matches the experimental data. This is also apparent from the distributions in Sec. IV A 3 and Appendix C.

3. Distributions of network characteristics

We now discuss the distributions of the network characteristics in ensembles of networks for the 2D models and the experimental data. We show the distributions of the clustering coefficient, transitivity, mean shortest-path length in

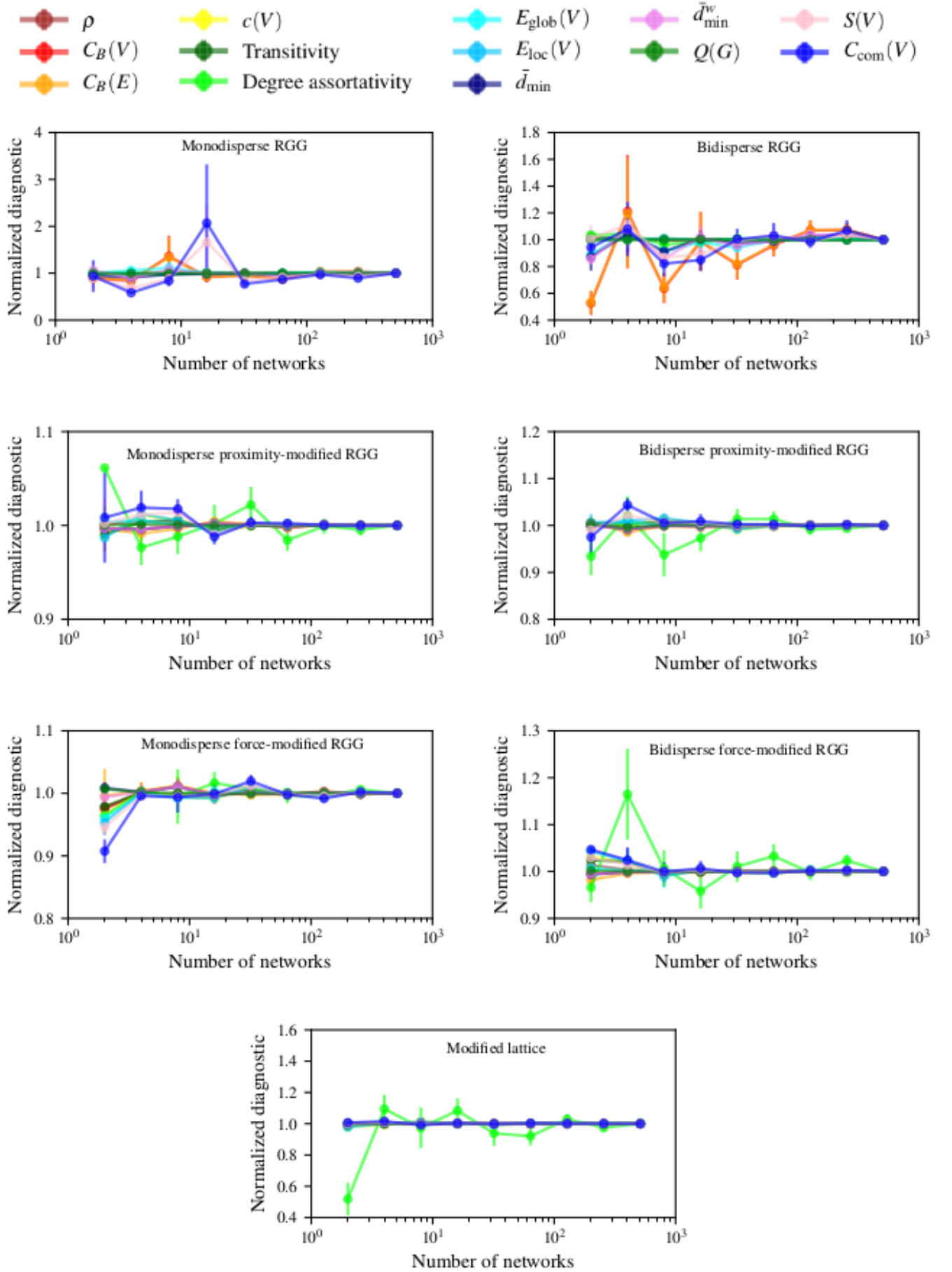


Figure 9. **Convergence characteristics of the diagnostics.** We show the mean diagnostic values and the corresponding error bars for ensembles with different numbers of networks. We normalize each diagnostic value by the mean that we compute from the largest ensemble of networks.

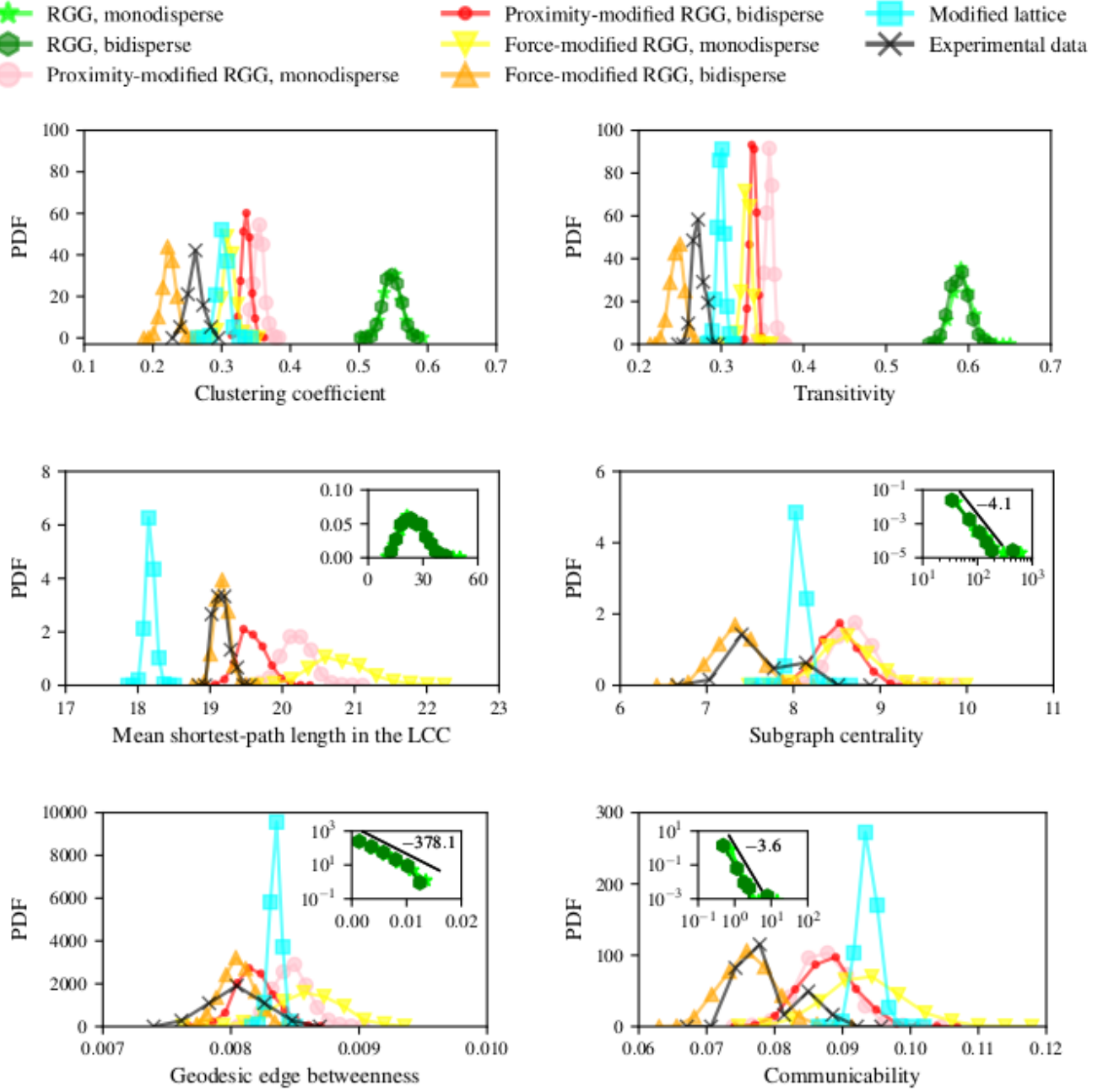


Figure 10. **Distributions of the diagnostics in the 2D models and the experimental data.** We show the distributions of the clustering coefficient, transitivity, mean shortest-path length in the LCC, subgraph centrality, geodesic edge betweenness, and communicability for the 2D models and the experimental data. We compute these distributions from the 1023 network realizations for each model and the 17 realizations for the experimental data. The black lines in the insets are guides to the eye that are based on power-law and exponential fits (using the method of least squares) of bidisperse diagnostic distributions. The corresponding numbers indicate the slopes of these lines.

the LCC, subgraph centrality, geodesic edge betweenness, and communicability in Fig. 10. We show the distributions of the other measures in Appendix C. In each plot, the black curve is the distribution of the experimental data.

The top panels of Fig. 10 suggest that the clustering coefficient and transitivity are useful measures for distinguishing between the unphysical and physical models. Specifically, the distributions of the RGG do not overlap with the distributions from the other models. Therefore, we can clearly distinguish between the RGG distributions and those of the other models. A closer look at the clustering coefficient and transitivity distributions also reveals that the

bidisperse force-modified RGG and the empirical granular networks have characteristics that are distinct from those of the other models. Based on these results, it is possible to distinguish these two network types from the proximity-modified RGGs and the monodisperse force-modified RGG. The modified-lattice distribution overlaps slightly with the one from the experimental data, although the two types of networks are rather distinct from each other based on visual inspection.

For the mean shortest-path length in the LCC, the experimental results are similar to those that we obtain for the bidisperse force-modified RGG. However, the distributions of the different models overlap more than those from the clustering coefficient and transitivity. Therefore, this does not yield a clear distinction between the two distributions.

The remaining three panels of Fig. 10 show the distributions of subgraph centrality, geodesic edge betweenness, and communicability. In the corresponding insets, we show the distributions of the RGG models and conclude that they differ qualitatively from the distributions of the other diagnostics. We can connect this observation to the convergence characteristics of subgraph centrality, geodesic edge betweenness, and communicability. To study the convergence characteristics, we compare the mean values of all diagnostics for different numbers of network realizations to the corresponding mean values in the largest ensemble (see Sec. IV A 1). For subgraph centrality, geodesic edge betweenness, and communicability in the unmodified RGGs, we find larger deviations of the mean diagnostic values in the smaller ensembles from the mean values in the largest ensemble than is the case for the other diagnostics (see Fig. 9). This observation is also reflected by the qualitatively different distributions of those diagnostics (see Fig. 10).

B. Diagnostics for 3D granular networks

We now briefly discuss the behavior of the diagnostic distributions for the 3D network models. We again focus on clustering coefficient, transitivity, mean shortest-path length in the LCC, subgraph centrality, geodesic edge betweenness, and communicability. We show the corresponding distributions in Fig. 11 and the remaining ones in Appendix C. For each model, we base the distributions on 256 network realizations.

The top panels in Fig. 11 show the distributions of the clustering coefficient and the transitivity. As in our 2D models, these two diagnostics are able to distinguish successfully between physical and unphysical models of granular networks. The only major difference between our results in 2D and 3D are the distributions (which we show in the insets in some panels) from the modified-lattice model. In 3D, the clustering coefficient and transitivity values for this model are to the left of the bidisperse force-modified RGG model.

For mean shortest-path length in the LCC, we observe that, in contrast to our observations in 2D, the distribution of the bidisperse proximity-modified RGG is to the left of the bidisperse force-modified RGG. Moreover, the distributions of the monodisperse and bidisperse force-modified RGG and the monodisperse proximity-modified RGG overlap more in 3D than in 2D. We also observe these differences between 2D and 3D in the distributions of geodesic edge betweenness. The distributions of subgraph centrality and communicability in 3D are qualitatively more similar to the ones in 2D than is the case for the other network diagnostics.

V. CONCLUSIONS AND DISCUSSION

We described and computed several common network diagnostics for a variety of 2D and 3D models of granular networks, ranging from unphysical ones with overlapping particles to physical ones that are free of overlaps. We studied the convergence properties of the diagnostics to identify a reasonable number of network realizations for the computation of the diagnostic distributions.

We examined the ability of the various network diagnostics to distinguish between physical and unphysical models of granular networks in 2D and 3D. Our results suggest that clustering coefficient and transitivity, which are related measures of triadic closure, are appropriate diagnostics to distinguish between the physical and unphysical models. The power of these two measures lies in the fact that their distributions for the different models are readily distinguishable from each other. In some cases, the diagnostics distributions of the 2D and 3D networks appear to satisfy markedly different statistical distributions, a phenomenon that we also expect to observe in comparisons of 2D and 3D granular networks from experiments.

Our results advance spatial random-graph models of granular networks and illustrate that simple modifications of random geometric graphs that incorporate a minimal amount of physics are useful models for gaining insights into granular and particulate networks.

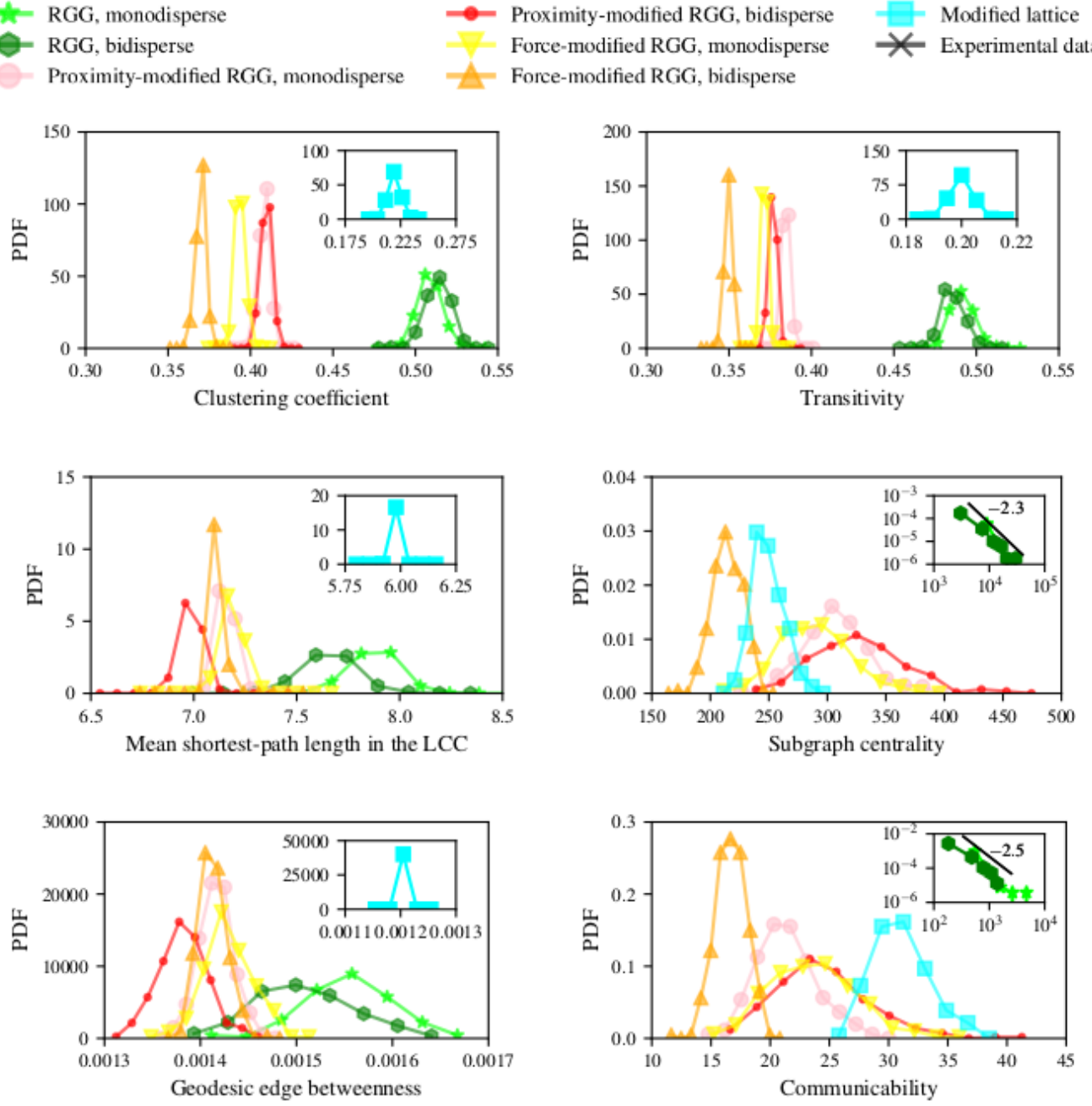


Figure 11. **Distributions of the diagnostics in 3D.** We show the distributions of the clustering coefficient, transitivity, mean shortest-path length in the LCC, subgraph centrality, geodesic edge betweenness, and communicability for the 3D models. We based the distributions on 256 network realizations for each model. The black lines in the insets are guides to the eye that we obtain from power-law fits (using the method of least squares) of the bidisperse diagnostic distributions. The corresponding numbers indicate the slopes of these lines.

ACKNOWLEDGMENTS

We thank Karen E. Daniels for providing the experimental granular network data [29]. We also thank David Kammer for the use of his cluster computing infrastructure and Kornel Kovacs for the cluster maintenance.

-
- [1] A. Smart, P. Umbanhowar, and J. Ottino, *Europhys. Lett.* **79**, 24002 (2007).
 - [2] A. Smart and J. M. Ottino, *Soft Matter* **4**, 2125 (2008).
 - [3] E. Berthier, M. A. Porter, and K. E. Daniels, arXiv preprint arXiv:1812.08025 (*PNAS*, in press) (2019).
 - [4] L. Papadopoulos, M. A. Porter, K. E. Daniels, and D. S. Bassett, *J. Complex Netw.* **6**, 485 (2018).
 - [5] H. J. Herrmann and S. Roux, *Statistical Models for the Fracture of Disordered Media* (Elsevier, Amsterdam, The Netherlands, 2014).
 - [6] T. L. Anderson, *Fracture Mechanics: Fundamentals and Applications* (CRC Press, Boca Raton, FL, USA, 2017).
 - [7] R. H. Heisser, V. P. Patil, N. Stoop, E. Villermaux, and J. Dunkel, *Proc. Natl. Acad. Sci. U.S.A.* **115**, 8665 (2018).
 - [8] M. E. Cates, J. P. Wittmer, J.-P. Bouchaud, and P. Claudin, *Chaos* **9**, 511 (1999).
 - [9] H. M. Jaeger, S. R. Nagel, and R. P. Behringer, *Rev. Mod. Phys.* **68**, 1259 (1996).
 - [10] B. Andreotti, Y. Forterre, and O. Pouliquen, *Granular Media: Between Solid and Fluid* (Cambridge University Press, Cambridge, UK, 2013).
 - [11] D. S. Bassett, E. T. Owens, M. A. Porter, M. L. Manning, and K. E. Daniels, *Soft Matter* **11**, 2731 (2015).
 - [12] M. Barthelemy, *Morphogenesis of Spatial Networks* (Springer International Publishing, Cham, Switzerland, 2018).
 - [13] J. Setford, *Models of granular networks in two and three dimensions* (2014), URL <http://www.math.ucla.edu/~mason/research/setford-final.eps>.
 - [14] J. Coon, C. P. Dettmann, and O. Georgiou, *Phys. Rev. E* **85**, 011138 (2012).
 - [15] C. P. Dettmann and O. Georgiou, *Phys. Rev. E* **93**, 032313 (2016).
 - [16] M. E. J. Newman, *Networks* (Oxford University Press, Oxford, UK, 2018), 2nd ed.
 - [17] A. Hagberg, D. Schult, and P. Swart (2019), URL <https://networkx.github.io/documentation/stable/index.html>.
 - [18] M. Girvan and M. E. Newman, *Proc. Nat. Acad. Sci.* **99**, 7821 (2002).
 - [19] M. E. J. Newman, *Phys. Rev. E* **67**, 026126 (2003).
 - [20] V. Latora and M. Marchiori, *Phys. Rev. Lett.* **87**, 198701 (2001).
 - [21] M. A. Porter, J.-P. Onnela, and P. J. Mucha, *Notices of the American Mathematical Society* **56**, 1082 (2009).
 - [22] S. Fortunato and D. Hric, *Physics Reports* **659**, 1 (2016).
 - [23] V. D. Blondel, J.-L. Guillaume, R. Lambiotte, and E. Lefebvre, *J. Stat. Mech.* **2008**, P10008 (2008).
 - [24] E. Estrada and J. A. Rodriguez-Velazquez, *Phys. Rev. E* **71**, 056103 (2005).
 - [25] E. Estrada and N. Hatano, *Phys. Rev. E* **77**, 036111 (2008).
 - [26] E. T. Owens and K. E. Daniels, *Europhys. Lett.* **94**, 54005 (2011).
 - [27] C. Chong, M. A. Porter, P. G. Kevrekidis, and C. Daraio, *J. Phys. Condens. Matter* **29**, 413003 (2017).
 - [28] R. P. Behringer and B. Chakraborty, *Rep. Prog. Phys.* **82**, 012601 (2018).
 - [29] D. S. Bassett, E. T. Owens, K. E. Daniels, and M. A. Porter, *Phys. Rev. E* **86**, 041306 (2012).

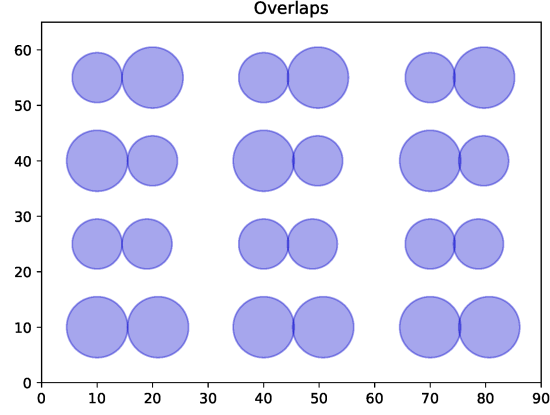


Figure 12. **Overlapping particles.** The left column shows particles with an overlap of $r_l/200$, where l indicates the particle on the left. In the middle column, the overlap is $r_l/20$; and in the right column, it is $r_l/15$.

Appendix A: Force-modified configurations

To obtain the potential-energy thresholds V^* (below which we no longer update particle positions) in Sec. III C, we consider the first term of Eq. 23 and set the distance between two neighboring particles k and l to be $r_k/200$. For simplicity, we consider the case in which every particle has 6 neighbors. In a monodisperse packing, we use 1022 particles of radius $r = 4.5$ mm to determine a value of the potential-energy threshold. In a bidisperse packing, we consider a system with 561 particles of radius $r_1 = 4.5$ mm and 561 with radius $r_2 = 5.5$ mm.

Supposing that the radii are unitless, the potential-energy thresholds are

$$\begin{aligned}
 V_{\text{mono}}^* &= \sum_k \sum_{l \neq k} \left[\frac{1}{2}(r_k + r_l) - \frac{1}{2}|\mathbf{x}_k - \mathbf{x}_l| \right]_+^{\beta+1} \\
 &= \sum_k 6 \times \left(\frac{r_k}{200} \right)^{\beta+1} = 1122 \times 6 \times \left(\frac{4.5}{200} \right)^{1.5} \\
 &\approx 22.7
 \end{aligned} \tag{A1}$$

for the monodisperse packing and

$$\begin{aligned}
 V_{\text{bi}}^* &= \sum_k \sum_{l \neq k} \left[\frac{1}{2}(r_k + r_l) - \frac{1}{2}|\mathbf{x}_k - \mathbf{x}_l| \right]_+^{\beta+1} \\
 &= \sum_k 6 \times \left(\frac{r_k}{200} \right)^{\beta+1} = 561 \times 6 \times \left(\frac{4.5}{200} \right)^{1.5} + 561 \times 6 \times \left(\frac{5.5}{200} \right)^{1.5} \\
 &\approx 26.7
 \end{aligned} \tag{A2}$$

for the bidisperse packing. In both cases, we set $\beta = 1/2$, which is the value that we used for our computations in Sec. III. These two values of the potential-energy threshold provide an estimate to assess the quality of network configurations that we generated using the force-modified RGG model. For 3D models, we take the number of neighbors of a particle to be 12. Therefore, the thresholds in 3D are $V_{\text{mono}}^* \approx 45.4$ and $V_{\text{bi}}^* \approx 53.4$.

We also examine the maximum overlap of our configurations. Based on visual inspection of Fig. 12, we conclude that an overlap of $r_k/200$ is sufficiently small. However, overlap distances of $r_k/20$ and $r_k/15$ are visible.

Appendix B: Diagnostic values

We present the numerical results for the diagnostics of the various models in Tables I and II.

Diagnostic	Experimental data		Modified lattice	
	Mean	Standard deviation	Mean	Standard deviation
Edge density	2.1288	0.0373	2.1284	0.0000
Geodesic node betweenness	0.0163	0.0002	0.0168	0.0001
Geodesic edge betweenness	0.0080	0.0002	0.0083	0.0000
Clustering coefficient	0.2613	0.0100	0.3019	0.0068
Transitivity	0.2714	0.0070	0.2994	0.0042
Degree assortativity	0.1377	0.0236	0.0648	0.0262
Global efficiency	0.0772	0.0005	0.0812	0.0003
Local efficiency	0.3301	0.0156	0.3886	0.0089
Mean shortest-path length in the LCC	19.1634	0.1069	18.1703	0.0585
Weighted mean shortest-path length	19.1483	0.1046	18.1456	0.0680
Maximized modularity	0.8712	0.0045	0.8487	0.0028
Subgraph centrality	7.6236	0.2958	8.0579	0.0678
Communicability	0.0790	0.0046	0.0937	0.0013
<hr/>				
Diagnostic	RGG (mono)		RGG (bi)	
	Mean	Standard deviation	Mean	Standard deviation
Edge density	2.1246	0.0439	2.1271	0.0469
Geodesic node betweenness	0.0057	0.0046	0.0059	0.0046
Geodesic edge betweenness	0.0028	0.0022	0.0029	0.0022
Clustering coefficient	0.5485	0.0126	0.5480	0.0121
Transitivity	0.5921	0.0119	0.5885	0.0113
Degree assortativity	0.5839	0.0398	0.5581	0.0409
Global efficiency	0.0225	0.0045	0.0232	0.0047
Local efficiency	0.6314	0.0128	0.6304	0.0127
Mean shortest-path length in the LCC	24.6106	6.4311	24.4985	6.2803
Weighted mean shortest-path length	15.9323	5.2432	15.9851	5.1460
Maximized modularity	0.9528	0.0032	0.9521	0.0033
Subgraph centrality	35.0580	29.4708	34.9849	19.7010
Communicability	0.4376	0.6047	0.4336	0.3419

Table I: **Network diagnostics of the experimental data, the 2D modified-lattice model, and the 2D RGG.** We average the results over 17 realizations for the experimental data and over 1023 realizations for the other models.

	Proximity-modified RGG (mono)		Proximity-modified RGG (bi)	
	Mean	Standard deviation	Mean	Standard deviation
Diagnostic				
Edge density	2.1226	0.0175	2.1298	0.0215
Geodesic node betweenness	0.0171	0.0002	0.0166	0.0002
Geodesic edge betweenness	0.0085	0.0001	0.0082	0.0001
Clustering coefficient	0.3540	0.0070	0.3356	0.0066
Transitivity	0.3584	0.0044	0.3389	0.0040
Degree assortativity	0.2799	0.0270	0.2179	0.0268
Global efficiency	0.0734	0.0006	0.0754	0.0006
Local efficiency	0.4663	0.0100	0.4430	0.0099
Mean shortest-path length in the LCC	20.1977	0.1987	19.5844	0.1852
Weighted mean shortest-path length	20.1808	0.2012	19.5716	0.1858
Maximized modularity	0.8754	0.0031	0.8670	0.0032
Subgraph centrality	8.6839	0.2133	8.5141	0.2257
Communicability	0.0874	0.0036	0.0879	0.0040

	Force-modified RGG (mono)		Force-modified RGG (bi)	
	Mean	Standard deviation	Mean	Standard deviation
Diagnostic				
Edge density	2.1317	0.0229	2.1183	0.0253
Geodesic node betweenness	0.0175	0.0004	0.0162	0.0001
Geodesic edge betweenness	0.0086	0.0002	0.0081	0.0001
Clustering coefficient	0.3106	0.0076	0.2238	0.0089
Transitivity	0.3311	0.0050	0.2463	0.0080
Degree assortativity	0.4404	0.0357	0.1952	0.0370
Global efficiency	0.0717	0.0010	0.0774	0.0004
Local efficiency	0.4172	0.0123	0.2789	0.0137
Mean shortest-path length in the LCC	20.7794	0.3931	19.1593	0.0938
Weighted mean shortest-path length	20.6838	0.4227	19.1463	0.0968
Maximized modularity	0.8659	0.0043	0.8410	0.0023
Subgraph centrality	8.6134	0.2818	7.3340	0.2270
Communicability	0.0934	0.0055	0.0760	0.0037

Table II: **Network diagnostics of the 2D proximity-modified RGG and the 2D force-modified RGG.** We average the results over 1023 realizations.

Appendix C: Additional diagnostic distributions

In Figs. 13 and 14, we show the distributions of the diagnostics that we did not show in Sec. IV.

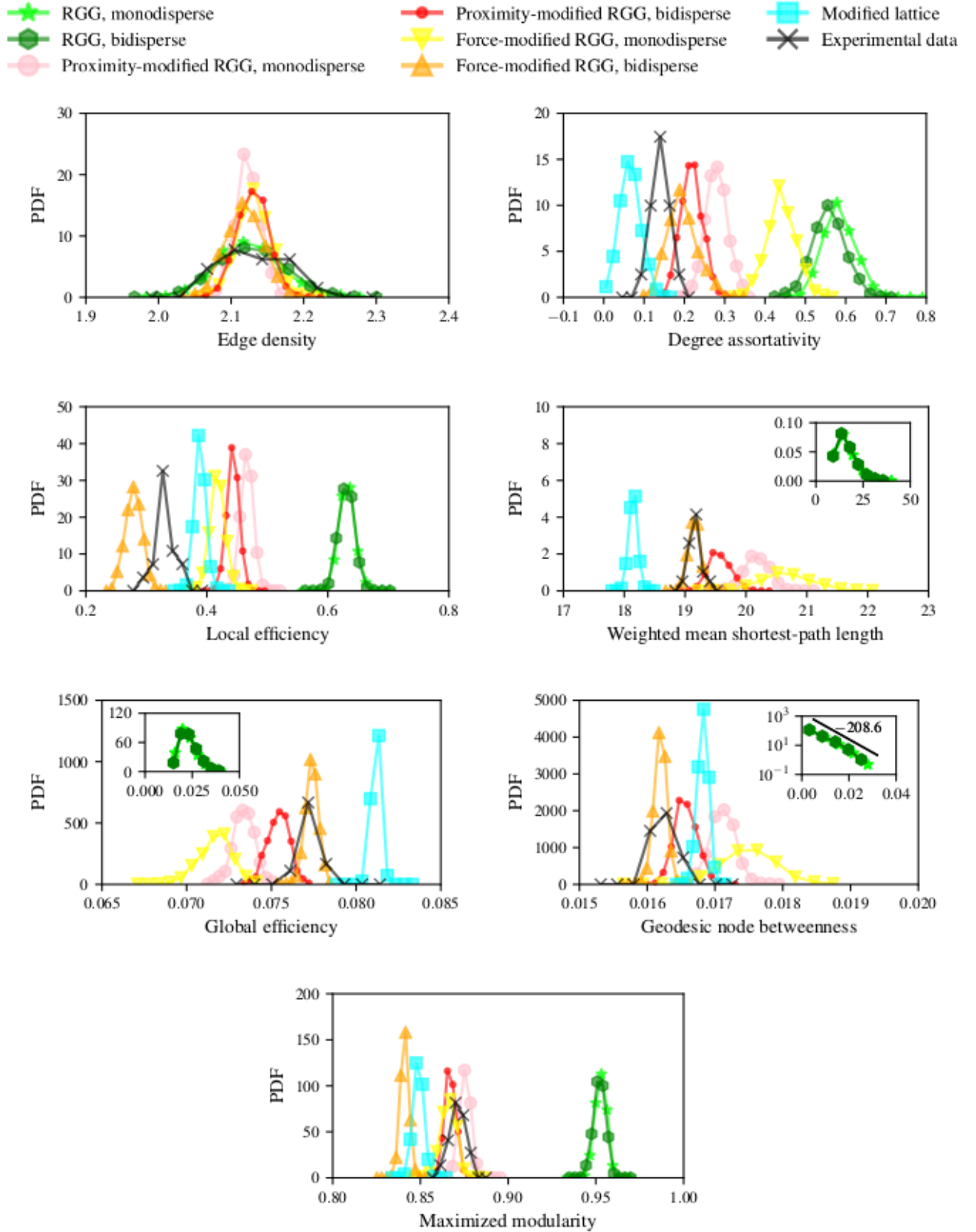


Figure 13. **Distributions of the remaining diagnostics in the 2D models and experimental data.** We show the distributions of edge density, degree assortativity, local efficiency, weighted mean shortest-path length, global efficiency, geodesic node betweenness, and maximized modularity for the 2D models and the experimental data. We determine the distributions from 1023 network realizations for each model and for 17 realizations for the experimental data. The black line in the inset of the geodesic-node-betweenness plot is a guide to the eye that we obtain from a power-law fit (using the method of least squares) of the bidisperse diagnostic distributions. The corresponding number indicates the slope of this line.

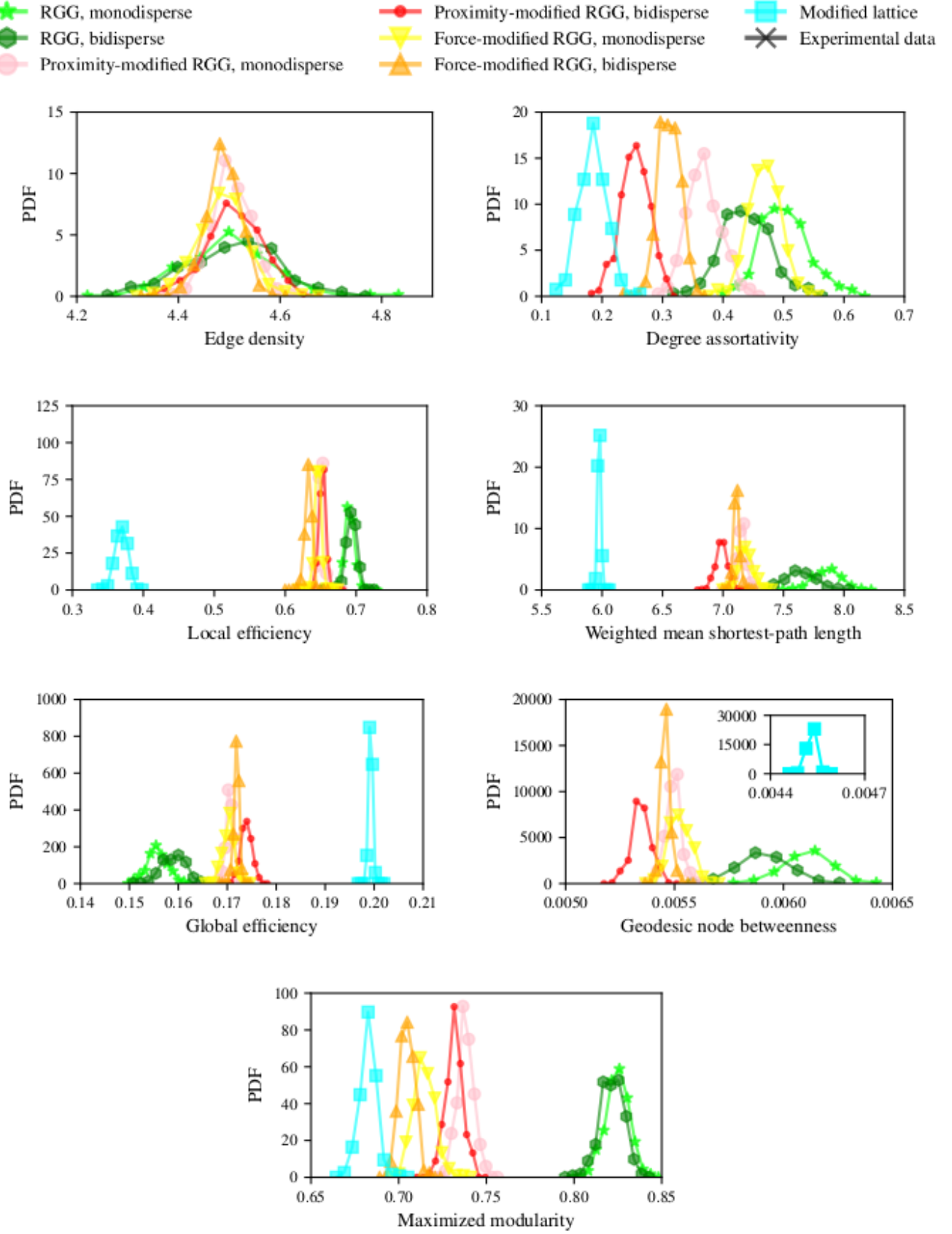


Figure 14. **Distributions of the remaining diagnostics in the 3D models.** We show the distributions of edge density, degree assortativity, local efficiency, weighted mean shortest-path distance, global efficiency, geodesic node betweenness, and maximized modularity for the 3D models. We determine the distributions from 256 network realizations for each model. In the plot of the edge-density distribution, we do not show the distribution of the modified-lattice model, because the edge density for this model always has exactly the same value.